THE FINITE-DIFFERENCE TIME-DOMAIN (FDTD) METHOD

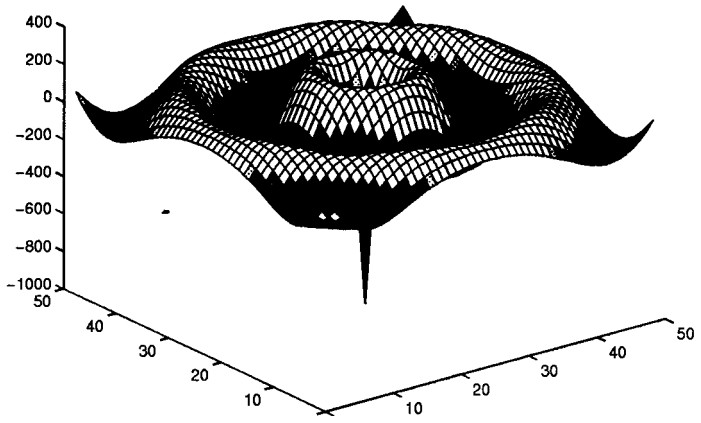

Applied to the analysis of crosstalk between parallel striplines

Edward Chan

June 10, 1996

0. INTRODUCTION

The impact of interconnects on circuit performance in both the analog and digital domains is ever increasing. No longer can interconnects be treated as mere delays or lumped RC networks. Crosstalk, ringing and reflection are just some of the issues that need to be understood then circumvented or utilized.

The most common simulation model for interconnects is the distributed RLCG model. Unfortunately, this model has many limitations which can lead to inaccurate simulations if not used correctly. This report uses the FDTD method to investigate crosstalk between transmission lines. The actual electromagnetic waves that propagate along striplines are computed allowing a direct, physical simulation of the coupling between striplines.

The results are compared to theoretical and HSPICE computations. While all three computations agree qualitatively, the magnitudes of the crosstalk signals are quite different. The HSPICE computation is incorrect because the calculated coupling parameters are too large. The FDTD results, on the other hand, are within 25% of theory and can be further improved by using finer discretizations.

The FDTD method produces useful and accurate results in the simple problem of analyzing crosstalk between parallel coplanar transmission lines. However, its distinguishing characteristic is its ability to simulate 3-D interconnect structures or structures exhibiting the skin effect. Since the FDTD method can be parallelized easily, this method is likely to be used to analyze ever more complex interconnects on massively parallel computers.

1. THE FDTD METHOD

1.1 Maxwell's equations

The FDTD method solves the time-dependent Maxwell's equations in one, two or three-dimensional source-free space. The essential equations are the curl equations

$$\nabla \times \boldsymbol{E} = -\frac{\partial \boldsymbol{B}}{\partial t} \tag{1.1.1}$$

$$\nabla \times \boldsymbol{H} = \frac{\partial \boldsymbol{D}}{\partial t} + \boldsymbol{J} \tag{1.1.2}$$

where $\boldsymbol{B} = [\mu]\boldsymbol{H}$, $\boldsymbol{D} = [\varepsilon]\boldsymbol{E}$ and $\boldsymbol{J} = [\sigma]\boldsymbol{E}$. In this work, $[\mu]$, $[\varepsilon]$ and $[\sigma]$ are assumed diagonal which imply that this version of the FDTD method can only handle linear media. In rectangular coordinates, these curl equations can be written out component-wise as

$$\frac{\partial H_x}{\partial t} = \frac{1}{\mu_x}\left(\frac{\partial E_y}{\partial z} - \frac{\partial E_z}{\partial y}\right) \tag{1.1.3}$$

$$\frac{\partial H_y}{\partial t} = \frac{1}{\mu_y}\left(\frac{\partial E_z}{\partial x} - \frac{\partial E_x}{\partial z}\right) \tag{1.1.4}$$

$$\frac{\partial H_z}{\partial t} = \frac{1}{\mu_z}\left(\frac{\partial E_x}{\partial y} - \frac{\partial E_y}{\partial x}\right) \tag{1.1.5}$$

and

$$\frac{\partial E_x}{\partial t} = \frac{1}{\varepsilon_x}\left(\frac{\partial H_z}{\partial y} - \frac{\partial H_y}{\partial z} - \sigma_x E_x\right) \tag{1.1.6}$$

$$\frac{\partial E_y}{\partial t} = \frac{1}{\varepsilon_y}\left(\frac{\partial H_x}{\partial z} - \frac{\partial H_z}{\partial x} - \sigma_y E_y\right) \tag{1.1.7}$$

$$\frac{\partial E_z}{\partial t} = \frac{1}{\varepsilon_z}\left(\frac{\partial H_y}{\partial x} - \frac{\partial H_x}{\partial y} - \sigma_z E_z\right). \tag{1.1.8}$$

The FDTD method solves these curl equations explicitly at each time step. Maxwell's divergence equations in source-free media, on the other hand, are implicitly obeyed by the formulation of the Yee cell (see section 1.2). It can be shown that the time derivative of the electric flux emanating from a cell in the FDTD space is

zero, which means that if we begin with zero flux, Gauss' law in source-free media, $\nabla \bullet \boldsymbol{D} = 0$, is satisfied for all time [1]. In the same way, the magnetic divergence law, $\nabla \bullet \boldsymbol{B} = 0$, is also satisfied.

1.2 Discretization in space and time

The 3-D FDTD simulation space is made up of cuboidal elements of sides Δx, Δy and Δz known as Yee cells. The six field components, E_x, E_y, E_z, H_x, H_y and H_z, are defined in each cell as shown in Fig. 1. Note that the field components are not all located at $(i\Delta x, j\Delta y, k\Delta z)$ but laid out in interleaved E-field and H-field grids. Each E-field component is encircled by 4 H-field components and vice-versa making the implementation of the curl equations obvious.

The common notation used to describe these fields is, for example

$$E_x^n[i, j, k] = E_x\left[\left(i + \frac{1}{2}\right)\Delta x, j\Delta y, k\Delta z\right]\Big|_{t = n\Delta t}, \qquad (1.2.1)$$

where *x* denotes the x-component, *n* significies that this is the value at the time-step n, whereas [i,j,k] indexes the Yee cell which contains this particular field. Refering to Fig. 1, we see that E_x[i,j,k] is actually located at $\left[\left(i + \frac{1}{2}\right)\Delta x, j\Delta y, k\Delta z\right]$.

It is important to remember that the fields are only defined at points on a grid, not throughout the entire cell. Intervening values have to be interpolated. The consitutive parameters, ε and μ, and the conductivity, σ, can be specified independently for each field component, allowing the simulation of linear anisotropic media. At material boundaries, the weighted average of these material parameters should be used. Each point can be considered to belong to 8 cuboids as shown in Fig. 2. Thus the parameter value should be

$$\zeta = \frac{\sum_{i=1}^{8} \zeta_i}{8} \qquad (1.2.2)$$

where ζ_i is the parameter for the surrounding cuboid *i*. For curved surfaces, the incorporation of a fuzziness factor in these parameters can lend smoothness to the otherwise staircase-like construction of objects out of Yee cells.

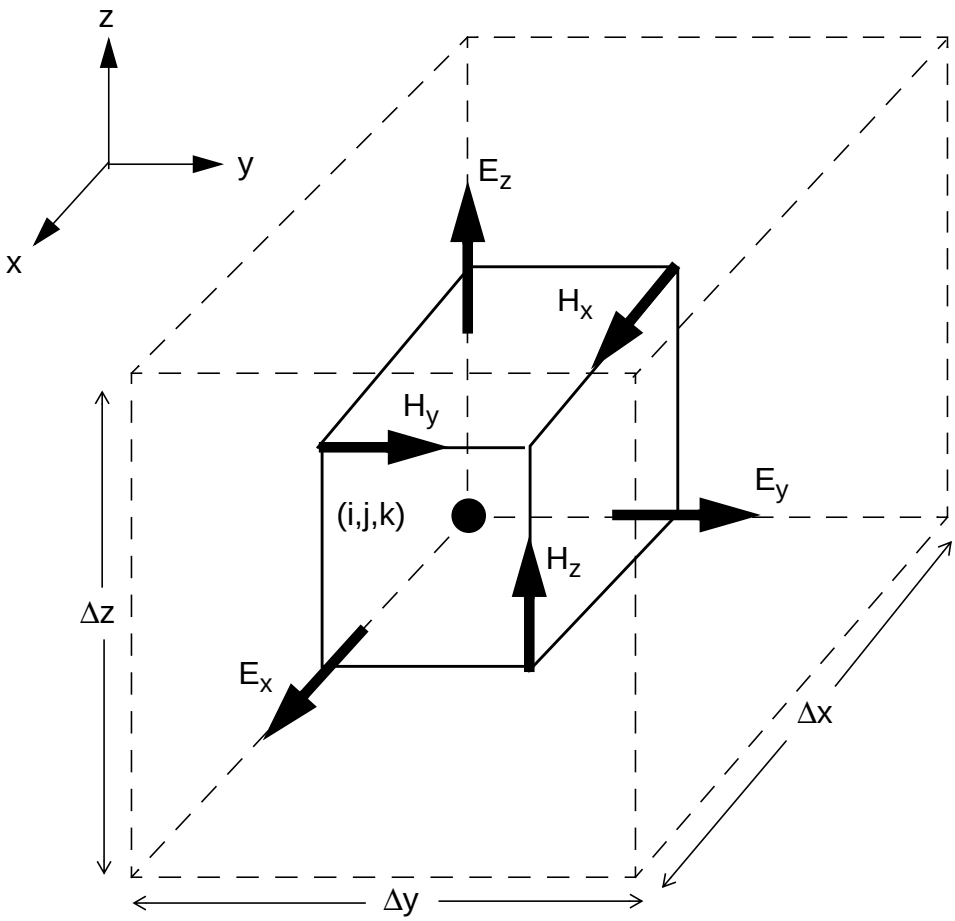

Fig. 1: The Yee Cell.

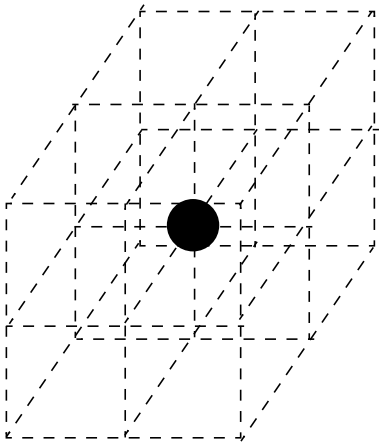

Fig. 2: Each point in the grid belongs to 8 cuboids.

Since the fields are only defined at points and each field component is specified at a different point, the shape of the structure is different for different field components. For example, in a 2-D mesh, a square defined for E_y is slightly displaced from that defined for E_x. Usually this poses no problems if we specify the material parameters (ε, μ, σ) for all the field points enclosed by the object. In Fig. 3, this requires specifying material parameters at four E_x locations and one E_y location if we wish to define the lower right square.

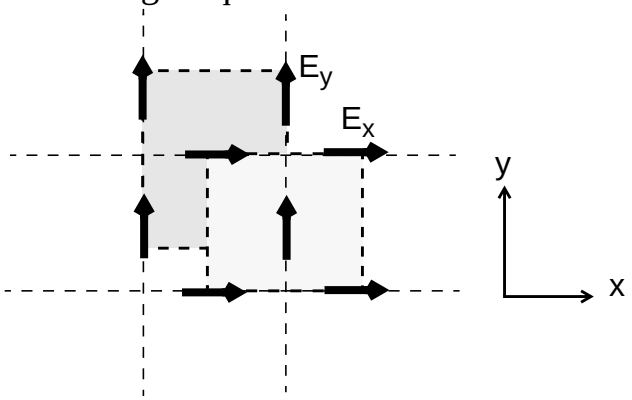

Fig. 3: Squares defined for E_x and E_y are displaced.

To obtain explicit update equations for the fields, we need to formulate the finite-difference approximations to the derivatives. For example, the 2nd-order accurate central difference approximation of H_x in time is

$$\frac{\partial}{\partial t}H_x^n[i,\,j,\,k] \;=\; \frac{H_x^{n+1/2}[i,\,j,\,k] - H_x^{n-1/2}[i,\,j,\,k]}{\Delta t} + O(\Delta t^2) \qquad (1.2.3)$$

whereas the the approximations in space of the corresponding curl are

$$\frac{\partial}{\partial z}E_y^n[i,\,j,\,k] \;=\; \frac{E_y^n[i,\,j,\,k+1] - E_y^n[i,\,j,\,k]}{\Delta z} + O(\Delta z^2) \qquad (1.2.4)$$

$$\frac{\partial}{\partial y}E_z^n[i,\,j,\,k] \;=\; \frac{E_z^n[i,\,j+1,\,k] - E_z^n[i,\,j,\,k]}{\Delta y} + O(\Delta y^2)\;. \qquad (1.2.5)$$

Note that all three equations approximate the derivatives at time t = n and position $\left[i\Delta x, \left(j+\frac{1}{2}\right)\Delta y, \left(k+\frac{1}{2}\right)\Delta z\right]$. If we plug these equations into

$$\frac{\partial H_x}{\partial t} = \frac{1}{\mu_x}\left(\frac{\partial E_y}{\partial z} - \frac{\partial E_z}{\partial y}\right) \tag{1.2.6}$$

we can obtain an explicit update equation for $H_x^{n+1/2}[i, j, k]$ using previous E-field and H-field components:

$$H_x^{n+1/2}[i, j, k] = \frac{\Delta t}{\mu_x}\left(\begin{array}{l}\dfrac{E_y^n[i, j, k+1] - E_y^n[i, j, k]}{\Delta z} \\ -\dfrac{E_z^n[i, j+1, k] - E_z^n[i, j, k]}{\Delta y}\end{array}\right) + H_x^{n-1/2}[i, j, k] \ . \tag{1.2.7}$$

Similar update equations can be obtained for the electric fields.

1.3 Leapfrog time-stepping

As shown in the previous section, H-fields are updated at $t = \left(n + \frac{1}{2}\right)\Delta t$ using the previous H-field at $t = \left(n - \frac{1}{2}\right)\Delta t$ and E-fields at $t = n\Delta t$. E-fields, on the other hand, are updated at $t = (n+1)\Delta t$ using the previous E-field at $t = n\Delta t$ and H-fields at $t = \left(n + \frac{1}{2}\right)\Delta t$.

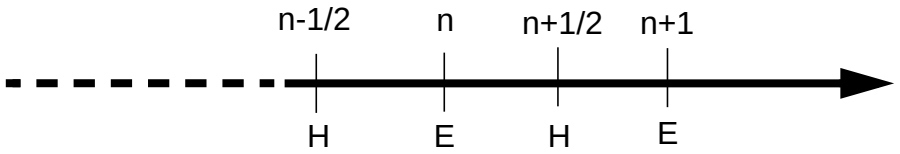

Fig. 4: Timeline showing when E and H fields are updated.

To remain numerically stable, the time-step must obey the Courant Stability Condition

$$\Delta t \le \frac{1}{c\sqrt{\frac{1}{(\Delta x)^2} + \frac{1}{(\Delta y)^2} + \frac{1}{(\Delta z)^2}}} \ . \tag{1.3.1}$$

To obtain good spatial resolution, the cell size should be less than a twentieth of the shortest wavelength

$$\Delta z \le \frac{\lambda_{min}}{20}. \tag{1.3.2}$$

1.4 Boundary Conditions

The simulation space must be terminated by boundary conditions pertinent to the problem because the central-difference equations for the E-fields cannot be applied at the boundary since the curl equation requires H-field values outside the boundary as shown in Fig. 5. H-fields at the boundary, however, are normal to the boundary so the curl is well-defined in terms of the tangential E-fields that exist right at the boundary.

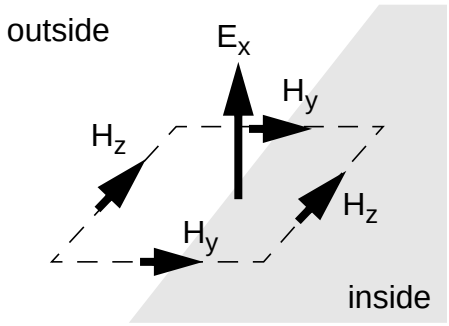

Fig. 5: Fields at the boundary of the simulation mesh.

The three common boundary conditions are the perfect electric conductor (PEC), perfect magnetic conductor (PMC) and the absorbing boundary condition (ABC). The PEC simply forces the tangential E-fields to zero, creating a perfectly reflecting wall (short circuit) for electric fields. The PMC forces the tangential H-fields to zero at the boundary. Since the tangential fields (H_z) are located half a cell into the simulation space as shown in Fig. 5, the fields right at the boundary are set to zero by conceptually placing H-fields of the same magnitude but of opposite sign half a cell outside the simulation space, forcing the interpolated value at the boundary to zero. The curl is now well-defined in terms of this conceptual H-field and the H-fields inside the simulation space. This boundary condition forces even symmetry about the PMC wall.

The third boundary condition attempts to simulate the situation of being in free space. Waves impinging on the boundaries are absorbed, much as if they simply kept on propagating without being reflected. The 1-D one-way wave equation

$$\left.\frac{\partial E}{\partial z} - \frac{1}{v}\frac{\partial E}{\partial t}\right|_{z=0} = 0 \tag{1.4.1}$$

will completely absorb a wave of the form *g(x,y)f(z+vt)* traveling in the negative z direction. However, physical or numerical dispersion will cause *v* to vary with frequency resulting in some reflection. Non-TEM modes, which have velocity of propagation less than *v*, will not be well-absorbed either. Fortunately, the homogeneous stripline supports pure TEM waves which are well-absorb by this boundary condition. Mur implemented this boundary condition, evaluated at $t = \left(n + \frac{1}{2}\right)\Delta t$ and $z = \frac{1}{2}\Delta z$, as shown below

$$\frac{\dfrac{E_y^{n+1}[i,j,1] + E_y^n[i,j,1]}{2} - \dfrac{E_y^{n+1}[i,j,0] + E_y^n[i,j,0]}{2}}{\Delta z} - \frac{1}{c}\left(\frac{\dfrac{E_y^{n+1}[i,j,1] + E_y^{n+1}[i,j,0]}{2} - \dfrac{E_y^n[i,j,1] + E_y^n[i,j,0]}{2}}{\Delta t}\right) = 0 \quad . \tag{1.4.2}$$

Since not all waves are incident normally on the boundaries, it is necessary to formulate 3-D one-way wave equations that will absorb oblique-incidence waves. By factoring the 3-D wave equation

$$\frac{\partial^2 E}{\partial x^2} + \frac{\partial^2 E}{\partial y^2} + \frac{\partial^2 E}{\partial z^2} - \frac{1}{c^2}\frac{\partial^2 E}{\partial t^2} = 0 \tag{1.4.3}$$

and taking the second order Taylor expansion to a square root term, we obtain the 2nd order 3-D one-way wave equation [1]

$$\left.\frac{\partial^2 E}{\partial z \partial t} - \frac{1}{c}\frac{\partial^2 E}{\partial t^2} + \frac{c}{2}\frac{\partial^2 E}{\partial x^2} + \frac{c}{2}\frac{\partial^2 E}{\partial y^2}\right|_{z=0} = 0. \tag{1.4.4}$$

This boundary condition works quite well as shown in Fig. 8, the example of a source in the center creating ripples propagating outwards to infinity. No interfer-

ence due to reflected waves is observed. Unfortunately, this boundary condition fails when used to terminate a stripline. As shown in Fig. 6, this ABC can only be used in the shaded region. If the ABC is used throughout the entire cross-section, it will generate longitudinal E-fields creating non-TEM modes and causing reflections of up to 80%.

Fig. 6: Region where 2nd order boundary conditions can be used.

We investigated possible causes for this behavior but the evidence does not support any of the possibilities. The impact of evanescent modes is ruled out because extending the simulated line length, and thus allowing the modes to die out, does not reduce the reflected wave. Numerical dispersion is not a factor either since using fourth-order central differencing, which reduces numerical dispersion by two orders of magnitude, produces no improvements. Neither does using a mesh 4 times denser along the x and y directions.

When Eq. 1.4.5 is truncated to

$$\left.\frac{\partial^2 E}{\partial z \partial t} - \frac{1}{c}\frac{\partial^2 E}{\partial t^2}\right|_{z=0} = 0 \tag{1.4.5}$$

it becomes equivalent to the first order equation. This truncated boundary condition works, which implies that the sum of the second derivatives,

$$\frac{c}{2}\frac{\partial^2}{\partial x^2}E + \frac{c}{2}\frac{\partial^2}{\partial y^2}, \tag{1.4.6}$$

should vanish but does not in the region just outside the strip (unshaded in Fig. 6).

1.5 Sources

Three types of sources are commonly used to excite fields in the simulation space: the wire source, the sheet source and the lumped circuit element source. Lumped elements are described in the next section.

The wire source, shown in Fig. 7, defines the E-field along a line in the simu-

lation mesh. Since the value of the field at the source is a fixed function of time, independent of its surroundings and reflections, it is a hard source and behaves like a PEC to incident waves. However, the reflections off a thin line are negligible. Fig. 8 shows the fields in the y-z plane emanating from the wire source of Fig. 7. Wire sources are used to simulate electric probe sources in waveguides.

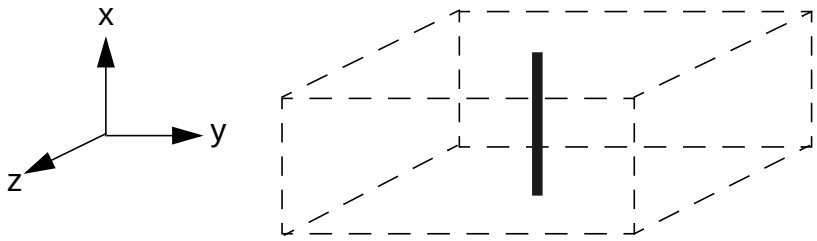

Fig. 7: Wire source.

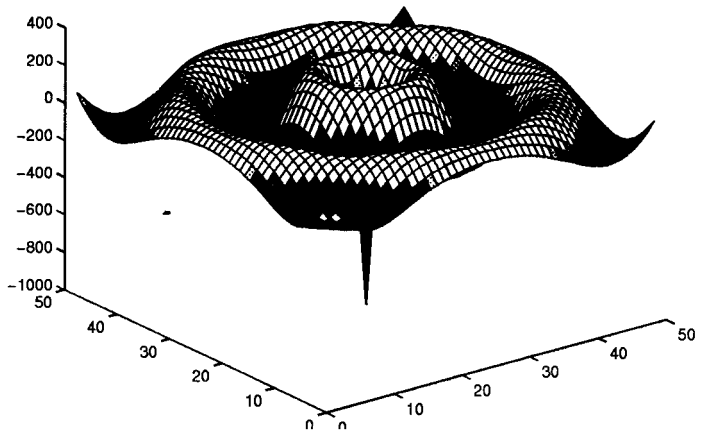

Fig. 8: E_x fields in the y-z plane.

However, sheet sources are more commonly used to excite waveguides because the resulting field pattern settles more quickly to the dominant propagating mode, thus reducing the required simulation space. The fields exciting a stripline are shown in Fig. 9. The stripline is fed antisymmetrically above and below the strip.

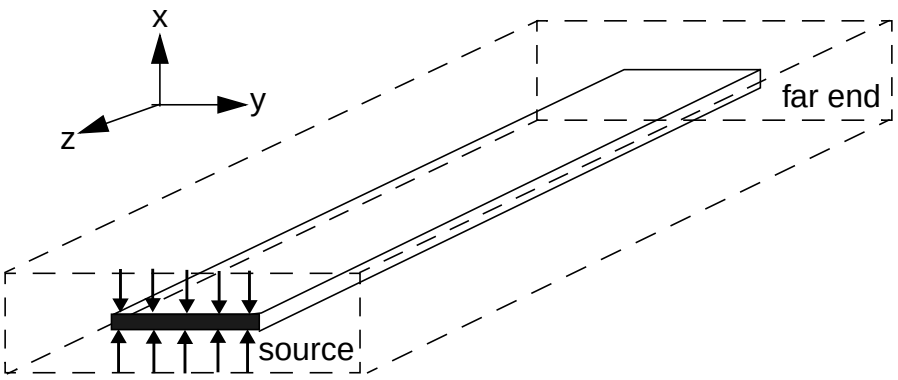

Fig. 9: Sheet source.

In this report, the fields in the source have uniform magnitude. If we desire to establish the dominant mode quickly, we can solve Poisson's equation, $\nabla^2 V = 0$, on the cross-section then pattern the source fields according to the computed field pattern. This, however, requires two simulation runs.

Since we are also fixing the field values, disregarding the surroundings, we need to be aware of reflections. We try to keep the source on as long as possible to allow the excitation, if it is of finite duration, to be generated smoothly. Abrupt terminations generate undesirable higher-order modes. Just before the wave reflected off the far end returns to the source, we turn on ABC's at the source to absorb the reflections.

A more realistic way to excite transmission lines is to use voltage sources, described in the next section.

1.6 Lumped circuit elements

We can modify the curl equations to include the effect of lumped circuit elements

$$\nabla \times \boldsymbol{H} = \frac{\partial \boldsymbol{D}}{\partial t} + \boldsymbol{J}_C + \boldsymbol{J}_L . \tag{1.6.1}$$

For a y-directed element in free space

$$J_L = \frac{I_L}{\Delta x \Delta z} \tag{1.6.2}$$

where I_L can be programmed arbitrarily to simulate resistors, capacitors, voltage sources, inductors, diodes and BJT's.

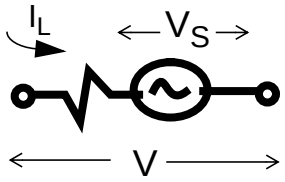

Fig. 10: Resistive voltage source.

For example, a resistive voltage source (Fig. 10) obeys Ohm's Law

$$I_L = \frac{V - V_S}{R_S}. \tag{1.6.3}$$

In finite-difference form, the equation becomes

$$I_L = \frac{\Delta y}{R_s}\left(\frac{E_y^{n+1} + E_y^n}{2}\right) - \frac{V_s^{n+1/2}}{R_s}. \tag{1.6.4}$$

A capacitor would obey the equation

$$I_L = \frac{C\Delta y}{\Delta t}(E_y^{n+1} - E_y^n). \tag{1.6.5}$$

In this crosstalk analysis, these lumped circuit elements are used to excite and terminate the striplines. For better uniformity, the strip is excited by antisymmetric banks of sources above and below the strip. The resistive loads are also placed above and below the strips although only one of each is used (Fig. 11).

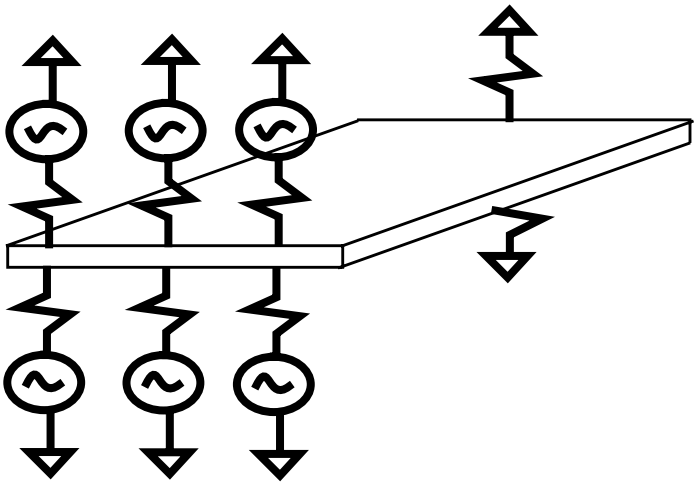

Fig. 11: Lumped element excitation and termination of a stripline.

1.7 Parameter Extraction

We would now like to extract useful circuit parameters from the fields. Fig. 12 shows the dimensions of the cross-section. We excited the stripline using a sheet source producing a Gaussian pulse: $\exp\left[-\left(\frac{t-50\Delta t}{13\Delta t}\right)^2\right]$. The bandwidth (between 5% points) is 22 GHz [2]. We turned on the source for $150\Delta t$, enough time for the pulse to be generated completely but not enough for the reflected pulse to arrive back at the source. We terminated the strip with 1st order ABC's which give reflections of less than 0.5%.

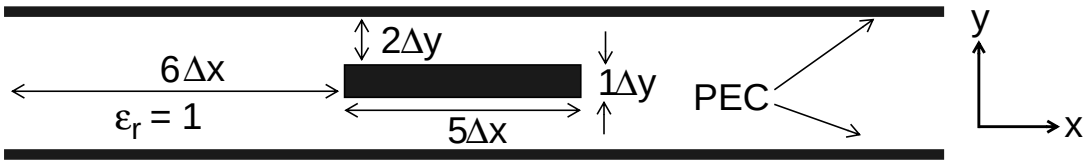

Fig: 12: Dimensions of the stripline being analyzed.
$\Delta x = \Delta y = \Delta z$ = 1mm, Δt = 1.925ps, line length = 100 Δz

The voltage as a function of time at a given position along z is

$$V(t) = \int E_y(t) \cdot dy \qquad (1.7.1)$$

where the integral is from the ground plane to the strip whereas the current is given

by

$$I(t) = \int H(t) \cdot dl \qquad (1.7.2)$$

where the integral is a loop around the strip as shown in Fig. 13. Figs. 14 and 15 show the voltage and current waveforms measured at $50\Delta z$.

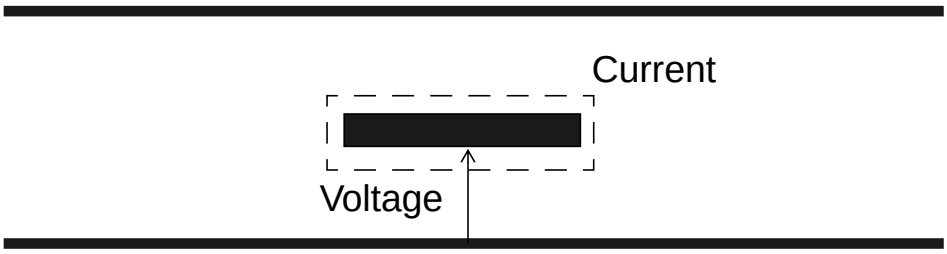

Fig. 13: Integration paths for voltage and current.

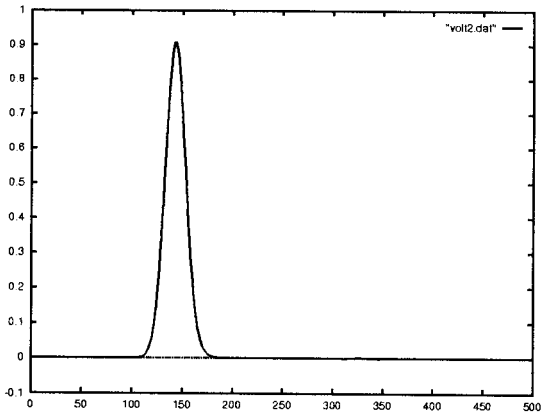

Fig. 14: V(t) at 50 Δz.

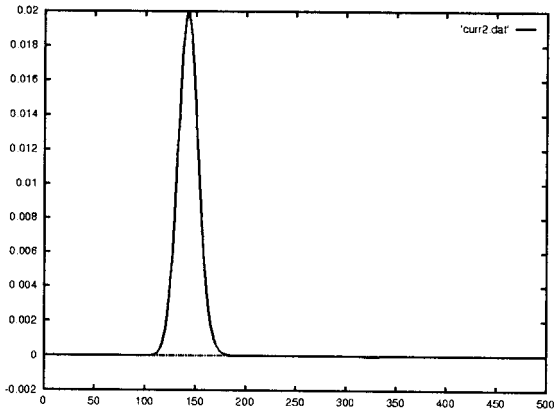

Fig. 15: I(t) at 50 Δz.

We obtain frequency domain information by performing the DFT on the

time-varying waveforms at various frequencies up to 22 GHz (the pulse bandwidth). The FFT is less suitable because the time step is so small that the resultant frequency range is too wide. The line impedance is defined as

$$Z_0 = \frac{DFT[V(t)]}{DFT[I(t)]} . \qquad (1.7.3)$$

For frequencies up to 22 GHz, the FDTD simulation gives a constant value of 45.7Ω. Table 1 shows line impedances extracted using other methods. This shows that the FDTD method is fairly accurate, and accuracy can be improved by simply increasing the density of the mesh at the expense of simulation time as shown by Becker [3]. Table 2 shows the Gaussian pulse guided by the stripline. The fields are slightly higher near the edges of the strip.

Table 1: Line Impedance Of Stripline

Method	Line Impedance (Ω)
FDTD (this report)	45.7
Becker (1x density)	45.7
Becker (2x density)	47.4
Becker (4x density)	48.0
MagiCAD	48.9
XFX	48.8
HSPICE	48.3

Table 2: E_y in the x-z plane

t = 100 Δt	t = 200 Δt	t = 300 Δt
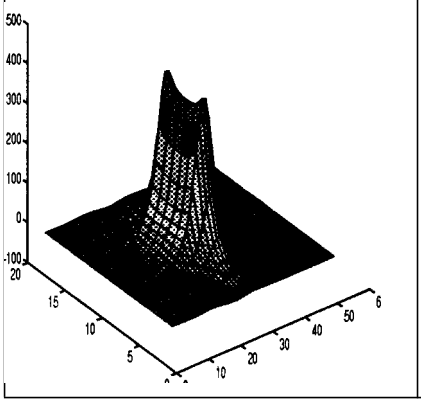	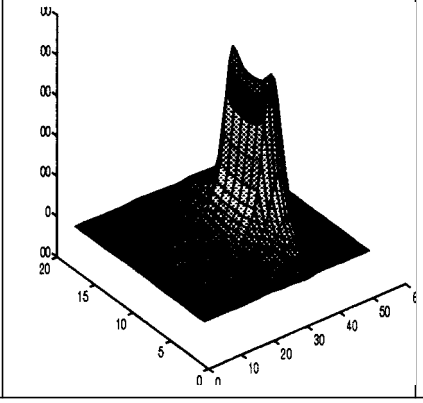	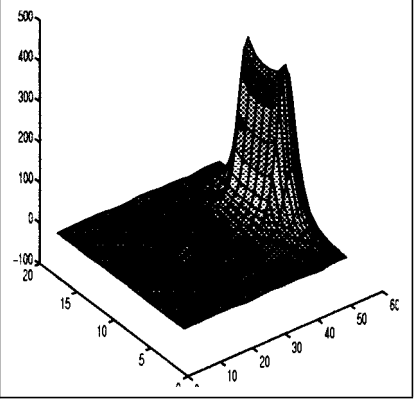

2. CROSSTALK BETWEEN TRANSMISSION LINES

2.1 Introduction

In a system consisting of two parallel striplines, shown schematically in Fig. 16, a signal propagating down one line (the active line) will generate a signal on the adjacent line (the passive line). This is a significant source of noise in digital circuits and is increasingly severe as signal rise times continue to decrease and routing densities increase.

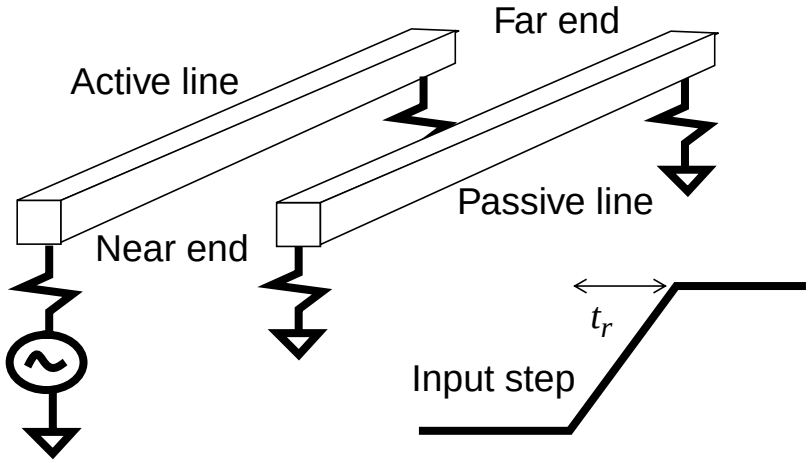

Fig. 16: Schematic drawing of two transmission lines in parallel.

The most common circuit model of this lossless coupled system is the distributed LC circuit shown in Fig. 17.

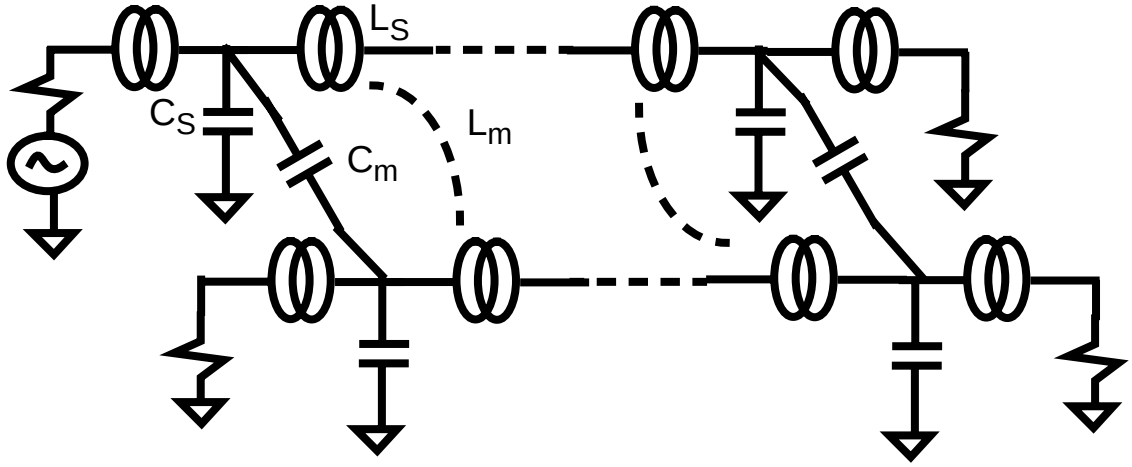

Fig. 17: Distributed LC circuit model of two coupled transmission lines.

C_S is the self-capacitance with respect to the ground plane whereas C_M is the mutual capacitance. L_S is the self-inductance of the line whereas L_M is the coupling inductance between the two lines. All these parameters are per unit length.

2.2 Theoretical Derivation of Crosstalk Between Loosely Coupled Lossless Transmission Lines

In a system of two identical parallel transmission lines, the Telegrapher's Equations can be modified to become [4]

$$-\frac{\partial I_1}{\partial x} = C\frac{\partial V_1}{\partial t} - C_m\frac{\partial V_2}{\partial t} \tag{2.2.1}$$

$$-\frac{\partial I_2}{\partial x} = -C_m\frac{\partial V_1}{\partial t} + C\frac{\partial V_2}{\partial t} \tag{2.2.2}$$

$$-\frac{\partial V_1}{\partial x} = L\frac{\partial I_1}{\partial t} + L_m\frac{\partial I_2}{\partial t} \tag{2.2.3}$$

$$-\frac{\partial V_2}{\partial x} = L_m\frac{\partial I_1}{\partial t} + L\frac{\partial I_2}{\partial t} \tag{2.2.4}$$

C is the *total* capacitance per unit length of the line. This is the C_{11} term -- the sum of the self-capacitance and the mutual capacitances -- in the capacitance matrix generated by field solvers.

Assume loose coupling, then take the Laplace transform to obtain

$$-\frac{\partial I_1}{\partial x} = sCV_1 \tag{2.2.5}$$

$$-\frac{\partial I_2}{\partial x} = sCV_2 - sC_mV_1 \tag{2.2.6}$$

$$-\frac{\partial V_1}{\partial x} = sLI_1 \tag{2.2.7}$$

$$-\frac{\partial V_2}{\partial x} = sLI_2 + sL_mI_1. \tag{2.2.8}$$

We can combine the equations to give

$$\frac{\partial^2 V_1}{\partial x} - \frac{s^2}{v^2}V_1 = 0 \tag{2.2.9}$$

$$\frac{\partial^2 V_2}{\partial x} - \frac{s^2}{v^2}V_2 = \frac{s^2}{v^2}\gamma(k-1)V_1 \tag{2.2.10}$$

where $\gamma = \frac{C_M}{C}$, $k = \frac{C_M}{C}\cdot\frac{L}{L_M}$ and $v = \frac{1}{\sqrt{LC}}$.

The first equation shows that the approximations completely decouple the active line signal from the passive line. Thus the signal on the active line propagates freely, as if in isolation. The passive line, described by the second equation, however, is driven by the active signal. The solution for the passive line when terminated by its characteristic impedance is

$$V_2 = \gamma\frac{V(k+1)}{4}\left[e^{-s\left(\frac{x}{v}\right)} - e^{-s\left(\frac{2l-x}{v}\right)}\right] - \gamma\frac{V(k-1)}{2}\left(\frac{x}{v}\right)(sV)e^{-s\left(\frac{x}{v}\right)}. \tag{2.2.11}$$

At the near end (x = 0), the solution simplifies to

$$V_2 = \gamma\frac{V(k+1)}{4}\left[1 - e^{-s\left(\frac{2l}{v}\right)}\right]. \tag{2.2.12}$$

The first term describes a scaled replica of the input whereas the second term describes the wave of opposite sign which cancels the initial wave after a delay of $\frac{2l}{v}$. At the far end (x = l),

$$V_2 = -\gamma \frac{V(k-1)}{2}\left(\frac{l}{v}\right)(sV)e^{-s\left(\frac{l}{v}\right)} \qquad (2.2.13)$$

which predicts that, after a delay of $\frac{l}{v}$, the scaled derivative of the input waveform will appear. These results are shown graphically in Table 3 along with results for other passive line terminations [5].

From the derivations, it is clear that the noise signals depend on the coupling strength, $\gamma = \frac{C_M}{C}$, which is 13.8 x 10^{-3} [6] for the stripline dimensions shown in Fig. 12 and separated by a distance 5Δx. Another parameter, $k = \frac{C_M}{C} \cdot \frac{L}{L_M}$, characterizes the homogeneity of the transmission line. For the homogeneous stripline, k = 1. Other important parameters are wave propagation speed (assuming TEM mode), *v*, rise time, t_r, and coupling length, *l*. In the following simulations, $v = 3 \times 10^8$ ms^{-1}, t_r = 100 ps, *l* = 60 mm and *l/v* = 200 ps. Using these values, the predicted waveforms are shown in the second column of Table 3. Note that since k = 1, the far end crosstalk signals are somewhat simplified since the (k-1) terms go to zero.

Table 3: Crosstalk between striplines (theoretical)

Passive Line Termination	Crosstalk between striplines (theoretical)	Computed Waveform Based on MagiCAD Parameters
Case #1 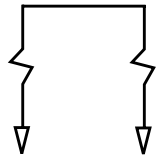	near end 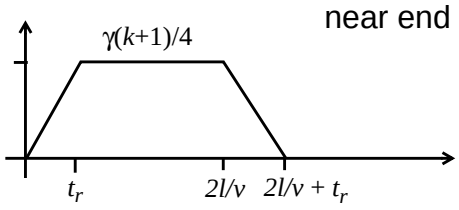 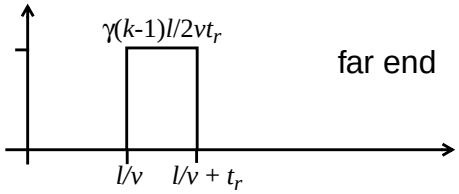	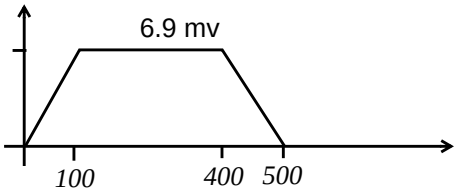 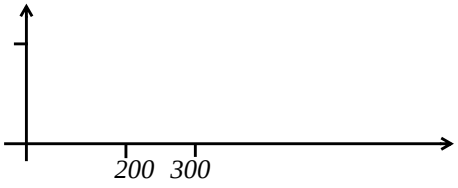
Case #2 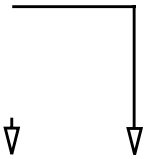	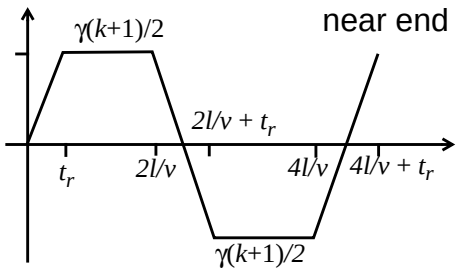	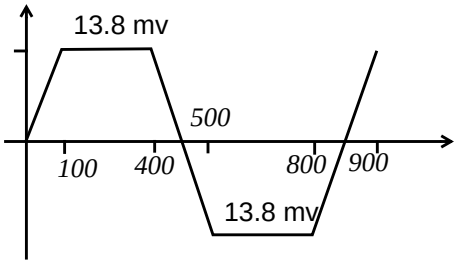
Case #3 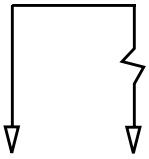	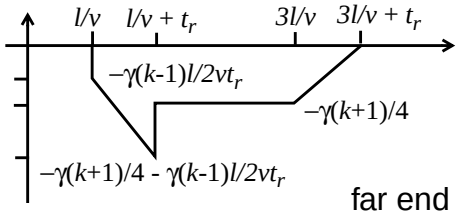	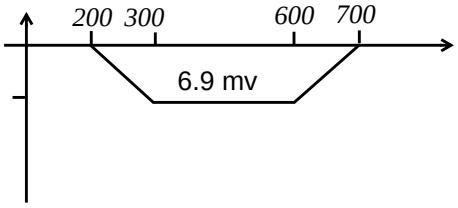

2.3 HSPICE Simulations

The HSPICE simulations used U-model striplines described by ELEV=1

(physical) parameters such as width, thickness, height and spacing. Since the element parameters (capacitance and inductance) are computed from analytic curve-fit equations, the parameters have limited ranges of validity. In this report, all the ratios of dimensions, width to thickness ratio for example, fall within the recommended ranges [7]. Thus, the errors in coupled line simulations are expected to be less than 15%. However, we found the errors to be much larger.

The gear integration method was used instead of the default trapezoidal method because it gives less dispersion and ringing when applied to a test simulation of a square pulse propagating down a single 100 cm distortionless stripline. 400 LC elements (lumps) were required to obtain good accuracy, many more than the default of 20 lumps. Fig. 18 shows the effect of the number of lumps and the methods of integration on the shape of the output pulse. We see that although the input pulse is the same for all three cases, the output pulses are quite different. Only the case with gear integration and 400 lumps exhibits no distortion whereas the other two cases show ringing and even undershoot. The results shown were obtained using HSPICE release 95.2 [8]. The latest 96.1 release improves the trapezoidal integration algorithm, reducing much of the ringing.

The resultant waveforms in the crosstalk simulations, using gear integration and 50 lumps, are shown in Table 4. The stripline cross-section is as described in Section 2.2 and shown in Fig. 12. The lines are each 60 mm long. We see that the waveforms have the expected shape and timing. However, the magnitude of the signals are about 150% larger than predicted by theory. A reason for this is the discrepancy in coupling parameters between those computed by MagiCAD and those used by HSPICE. Table 5 compares those critical parameters.

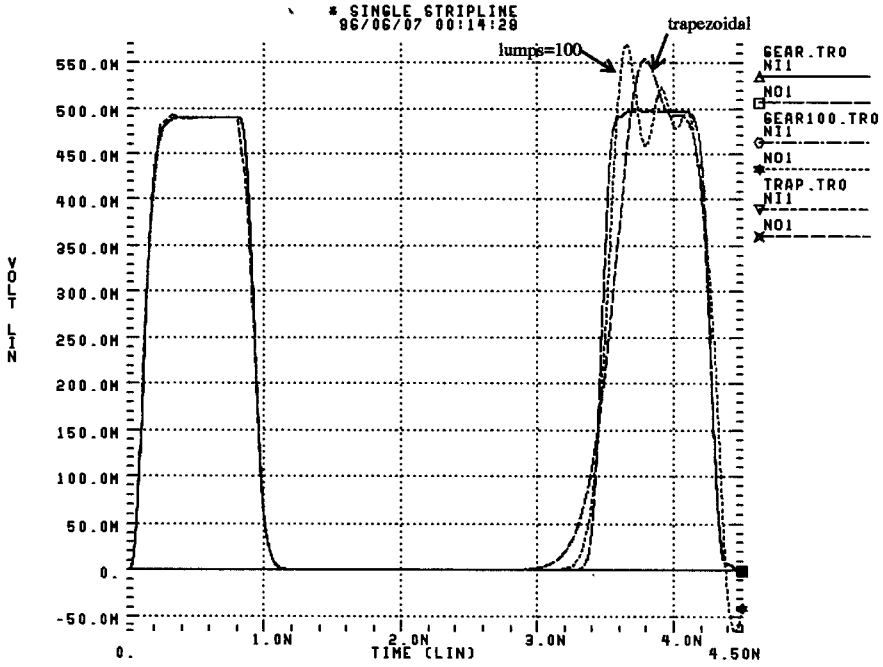

Fig. 18: Square pulse propagating down a distortionless stripline. Rise time = 100 ps, Line length = 100 cm, Step size = 1 ps

Table 4: HSPICE and FDTD computation of crosstalk

Passive Line Termination	HSPICE computation	FDTD computation
Case #1 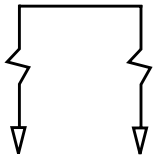	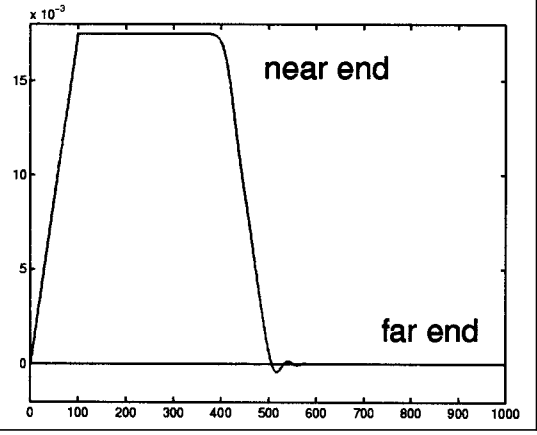	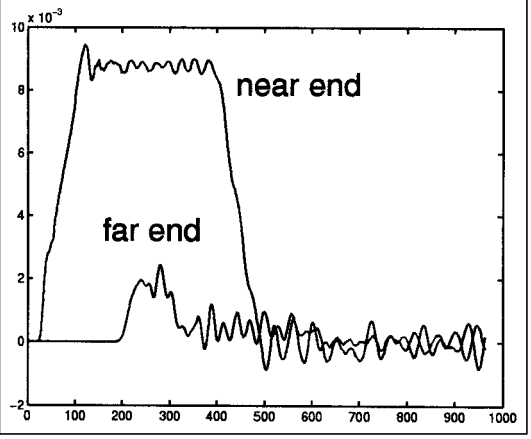

Table 4: HSPICE and FDTD computation of crosstalk

Passive Line Termination	HSPICE computation	FDTD computation
Case #2 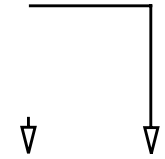	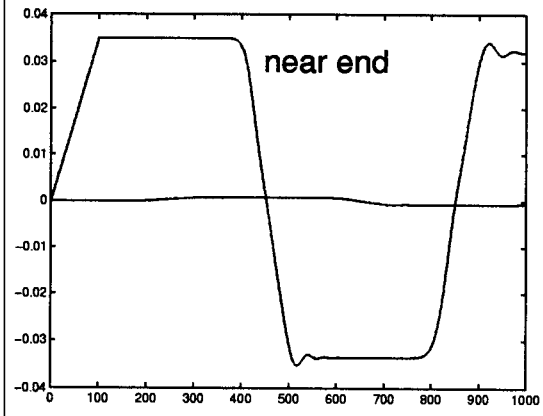	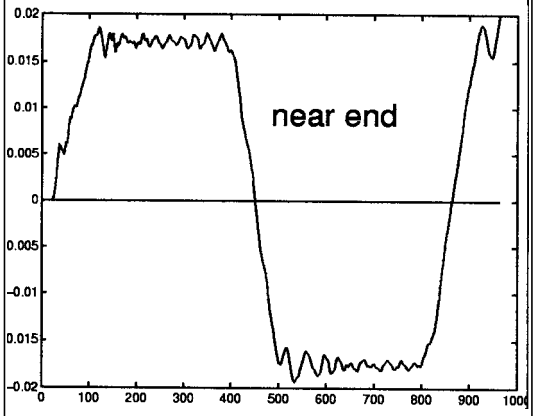
Case #3 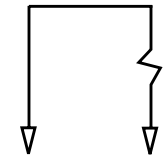	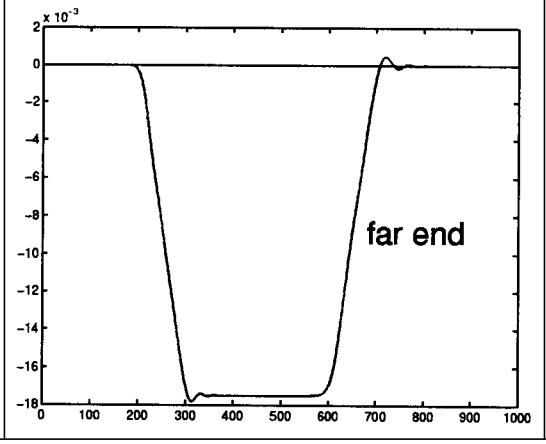	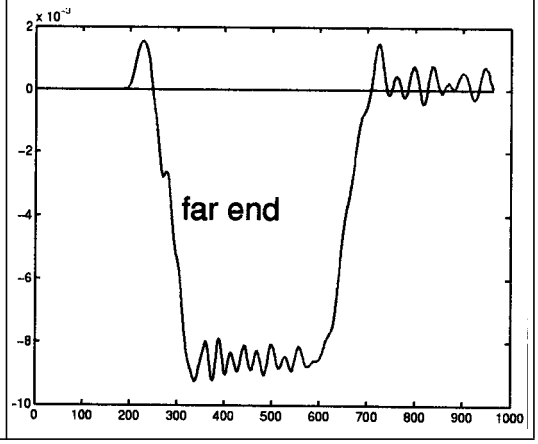

Table 5: Distributed LC circuit parameters

Parameter	MagiCAD	HSPICE	% difference
Total capacitance (pF/m)	67.8	69.1	+2.0
Coupling capacitance (pF/m)	0.933	2.42	+159
Self inductance (nH/m)	162	161	-0.6
Mutual inductance (nH/m)	2.20	5.63	+156

2.4 FDTD Simulations

The FDTD simulations used exactly the same stripline dimensions described in Section 2.3 for the HSPICE simulations. The simulated waveforms are shown alongside the HSPICE waveforms in Table 4. Once again, the crosstalk signals agree qualitatively with theory but are a little larger in magnitude (about 25% larger).

By quadrupling the mesh density in every dimension, we can obtain more accurate results as shown in Fig. 19. We see here that the crosstalk magnitude is very close to that predicted by theory (within 2%) . However, the simulation takes at least 256 times longer to run because the step sizes in all 4 dimensions, including time, are reduced by a factor of 4.

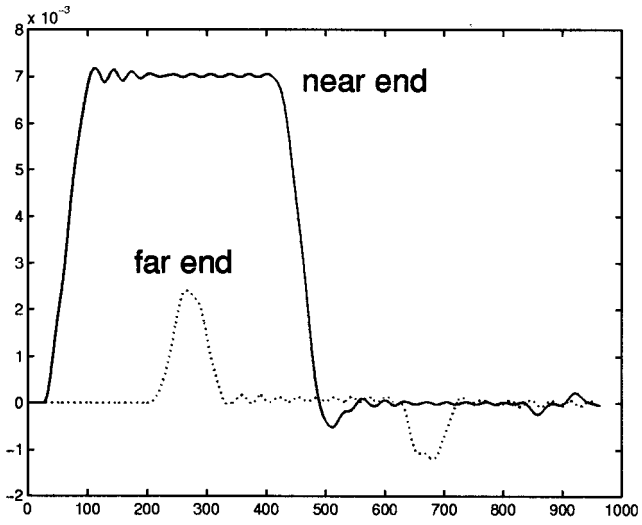

Fig. 19: Case #1 crosstalk waveforms simulated using a quadruple density FDTD mesh and a raised cosine excitation.

The waveforms are also very noisy because of the abruptness of the piece-wise linear step input. A raised cosine input will reduce the amount of noise. Fig. 19 also shows the effect of using a raised cosine excitation. However, the rise time of a raised cosine function is not well defined and thus results cannot be directly compared to theoretical computations.

The crosstalk signals are delayed by about 20 ps due to wave retardation

(waves require a finite amount of time to traverse the spacing between lines). This effect is not captured by the HSPICE simulations. Also, a far end crosstalk signal is observed even when the passive line is terminated by its charateristic impedance (Case #1). This is due to an additional fringe capacitance (Fig. 20) of about 16fF at the near end that disrupts homogeneity and generates separate capacitive and inductive waveforms that do not cancel out at the far end.

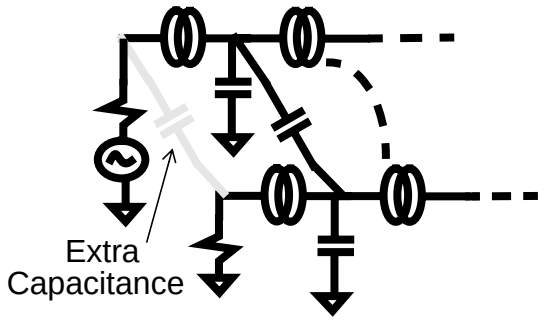

Fig. 20: Extra fringing capacitance at the near end.

2.5 Observations

Table 6: Comparison between HSPICE and FDTD

HSPICE	FDTD
Good agreement of waveform shape and timing with theory.	Good agreement of waveform shape and timing with theory.
Poor agreement in magnitude of crosstalk (150% larger than theory) due to incorrect coupling parameters.	Reasonable agreement in magnitude of crosstalk (25% larger than theory). Accuracy improves with mesh refinement (within 2% with quadruple density mesh).
Can filter input step to prevent unrealistic ringing.	Difficult to filter input therefore output is noisy. But can use raised cosine.
2.3 user secs on HP 9000/700 using 50 lumps.	17 user secs on HP 9000/700 using single density mesh. 74 min 52 secs using quadruple density mesh.

Table 6: Comparison between HSPICE and FDTD

HSPICE	FDTD
Easy to set up, modify and inspect results. Commercial GUI.	Difficult to set up, modify grid or parameters, and inspect results. Custom C program. XFDTD by Remcom Inc. is a possibly viable commercial product.
No retardation (delay) effect.	Crosstalk is retarded (delayed).
No effect of fringing.	Fringing capacitance at the near end causes a pulse at the far end.
Does not model modal dispersion correctly (RLCG model cannot handle non-TEM modes).	No difficulty with higher-order modes, except that the definition of voltage and current becomes ambiguous.
Two-dimensional (uniform) structures.	Three-dimensional structures. Can handle vias, fan out and other discontinuities.
All parasitics have to be included explicitly.	Models reality.
Can only handle regular systems with ratios of dimensions within the allowed range.	Can model any system, even conductors of irregular geometry.
Cannot simulate frequency-dependent effects (including skin effect).	Can simulate frequency dependent effects such as skin effect and complex dielectric loss.

3. CONCLUSIONS

For most users, HSPICE modeling of crosstalk is fast and adequate (once the coupling parameters are corrected), except when frequency-dependent effects are important, coupling is weak or conductors are irregular or 3-D in nature. The FDTD method distinguishes itself when lumped circuits and distributed circuits are inadequate. The challenge is to determine when the extra information provided by the

FDTD method is worth the added complexity and computation cost.

User's of both the FDTD method and HSPICE need to always be aware of the limitations of the simulators especially concerning discretization. Finer meshes or smaller lumps usually improve accuracy at the expense of computation time. However, HSPICE can suffer convergence problems if too many lumps are used.

The FDTD domain is easily partitioned, making it ideal for parallelization. Each partition can be computed independently. Boundary values (between partitions) only need to be exchanged at the end of each computation time step. As computing costs decrease, the use of the FDTD method to aid signal integrity verification will continue to expand.

REFERENCES

[1] A. Taflove, "Computational Electrodynamics," *Artech House*, 1995.

[2] X. Zhang and K.K. Mei, "Time-Domain Finite Difference Approach to the Calculation of the Frequency-Dependent Characteristics of Microstrip Discontinuties," *IEEE Trans Microwave Theory and Techniques*, vol 36 no 12, Dec 1988, pp 1775-1787.

[3] W.D. Becker, "The Application of Time-Domain Electromagnetic Field Solvers to Computer Package Analysis and Design," Ph.D. Thesis, University of Illinois at Urbana-Champaign, 1993.

[4] D.B. Jarvis, "The Effects of Interconnections on High-Speed Logic Circuits," *IEEE Trans Electronic Computers*, Oct 1963, pp 476-487.

[5] J.A. DeFalco, "Reflection and Crosstalk in Logic Circuit Interconnections," *IEEE Spectrum*, Jul 1970, pp 44-50.

[6] MagiCAD 2.1.0, Mayo Foundation, Special Purpose Processor Development Group.

[7] HSPICE 96.1 User's Manual, Meta Software, Inc.

[8] HSPICE 95.2, Meta Software, Inc.